Computational Analysis of Threonine Ladders on Distinct Beta-Solenoid Scaffolds, with Implications for the Design of Novel Antifreeze Proteins

Cianna N. Calia[*,†] and Francesco Paesani[*,†,‡,¶,§]

†*Department of Chemistry and Biochemistry, University of California San Diego, La Jolla, California 92093, United States*

‡*Materials Science and Engineering, University of California San Diego, La Jolla, California 92093, United States*

¶*Halicioğlu Data Science Institute, University of California San Diego, La Jolla, California 92093, United States*

§*San Diego Supercomputer Center, University of California San Diego, La Jolla, California 92093, United States*

E-mail: ccalia@ucsd.edu; fpaesani@ucsd.edu

Abstract

Cold-adapted organisms frequently express antifreeze proteins (AFPs) that facilitate their survival at low temperatures, with some especially potent insect AFPs exhibiting beta-solenoid structures with ice-binding threonine ladders. Beta-solenoids exist in nature in numerous forms and emerging protein design technologies may afford opportunities to diversify them further, suggesting the possibility of creating a variety of new AFPs by installing a threonine ladder on non-AFP natural or designed beta-solenoids. However, early attempts at such engineering, combined with differences observed between AFPs and structurally similar ice-nucleating proteins, have raised a critical question: Does the specific solenoid scaffold significantly affect a threonine ladder's structural characteristics (and thus its suitability for ice binding)? We set out to address this question by creating distinct variants of a model beta-solenoid for *in silico* analysis via structure prediction and molecular dynamics simulations. Our findings indicate that the concavity of the beta-solenoid face on which a threonine ladder is arrayed can substantially influence the local geometry of the threonines, with less concave examples resembling the AFP TmAFP and a more concave example losing the ordered channel waters present in well-studied natural ice-binding surfaces. Disparities in concavity and threonine hydroxyl spacings appeared initially in our AlphaFold results and were supported by the simulations, illustrating AlphaFold's possible utility for high-throughput preliminary screening of designed beta-solenoid AFP sequence candidates. We demonstrate this utility by using AlphaFold to evaluate sequences generated by the state-of-the-art inverse folding tool ProteinMPNN that can potentially be transformed into novel hyperactive AFPs to support applications ranging from biomedical cryopreservation to food science.

Introduction

Antifreeze proteins (AFPs) are a key survival mechanism for a variety of organisms adapted to icy environments, from psychrophilic microbes to polar fish and overwintering insects and plants.[1–4] A class of ice-binding proteins (IBPs), AFPs can exert control over ice growth in multiple ways: They lower the freezing temperature by binding to ice crystals and inducing curvature that raises the free energy of the ice phase (thermal hysteresis via the Kelvin effect),[5–7] and they also reduce the formation of large ice crystals at the expense of smaller ones (ice recrystallization inhibition).[8,9] These forms of activity make AFPs a promising technological solution for applications such as cryopreservation of cells, tissues, and organs for research and medical use;[10–15] protection of crops from frost damage;[16–19] and texture modulation in foods such as ice cream.[20–23]

AFPs exhibit a range of different structures, such as a single alpha helix in the type I AFP from winter flounder,[24] a small globular fold in the type III AFP from ocean pout,[25] and beta-solenoid structures in hyperactive insect AFPs.[26,27] All known AFPs are believed to possess an ice-binding surface (IBS), though the nature of the IBS varies with AFP type. Hyperactive insect AFPs such as TmAFP (from the mealworm beetle *Tenebrio molitor*) and sbwAFP (from the spruce budworm *Choristoneura fumiferana*), which have especially potent thermal hysteresis activity,[28,29] have aligned threonine-X-threonine (TXT) motifs in the consecutive loops of their beta-solenoid structures, forming a flat face with two rows of threonine residues — a threonine ladder IBS[26,27,30] (Figure 1A). Numerous studies have identified ordered water molecules, such as channel waters between the threonine rows, as an additional and salient feature of the IBS (e.g., Refs. 26,31–41).

The relative simplicity of the TXT motif and the high thermal hysteresis activity of insect AFPs together suggest that the threonine ladder may be an ideal IBS for use in developing novel AFPs to diversify the set of ice-binding biomolecules available for various applications. For instance, transplanting the threonine ladder IBS onto alternative beta-solenoid scaffolds that are not stabilized by disulfide bonds presents a potential way to obtain highly active new

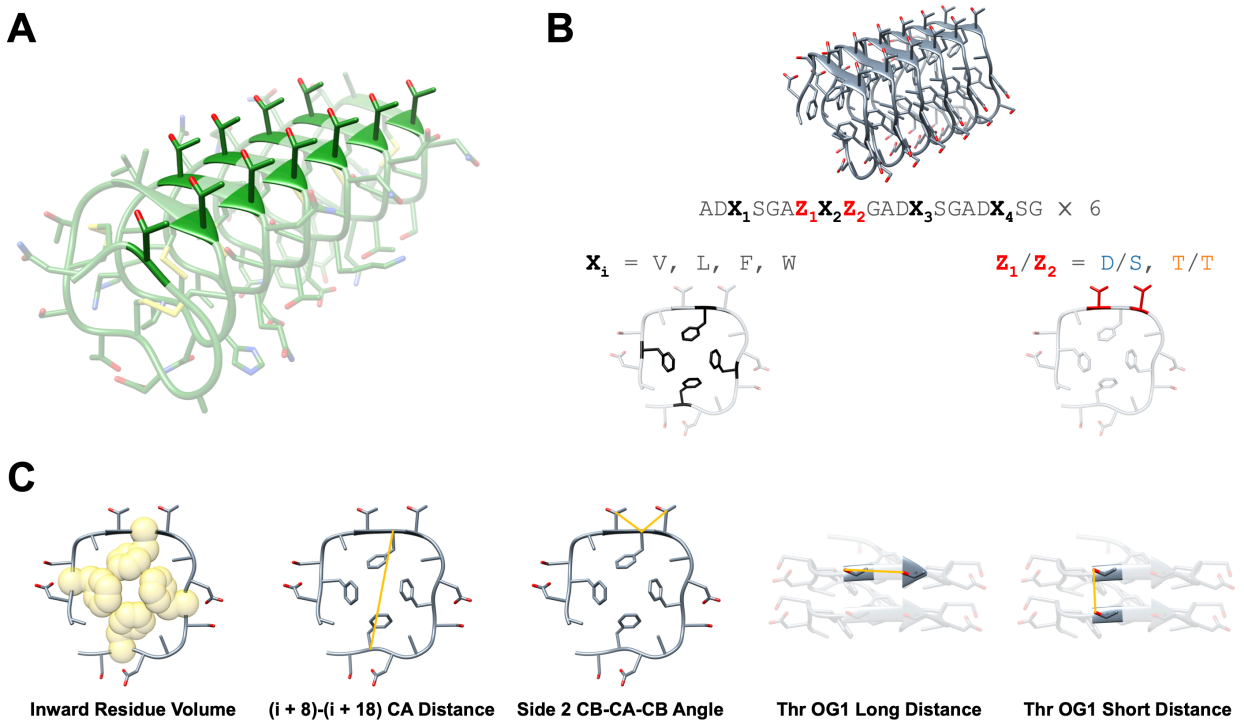

Figure 1: (A) Crystal structure of TmAFP (PDB 1EZG), with IBS threonines highlighted in darker green. (B) Overview of our construction of model beta-solenoid sequences based on pentapeptide repeat proteins. (C) Visual outline of the key features relevant to our analysis of predicted structures and simulations.

AFPs without the expression challenges associated with insect AFPs that rely on extensive disulfide bonding for stability.[42] With the recent explosion of deep learning methods for protein design and structure prediction (e.g., Refs. 43–53), even more creative possibilities for AFP/IBP design and optimization are now also within reach. However, whether a threonine ladder can function equally well as an IBS on distinct scaffolds, either natural or designed, that did not evolve for this role remains an open question. In addition, it is so far unclear how cutting-edge protein design methods, most of which do not explicitly address water, can take advantage of the sizable body of research establishing the crucial role of water ordering in the function of biological ice-binding motifs.

Pentapeptide repeat proteins are a class of bacterial proteins that have beta-solenoid structures with a square profile. Each square loop has four sets of five residues; the inward-facing residue in the middle of each side is typically leucine or phenylalanine.[54,55] Importantly,

pentapeptide repeat proteins have relatively flat faces, do not require disulfide bonding for stabilization, and tolerate a variety of different residues in their outward-facing positions.[56] These properties make pentapeptide repeat proteins a promising choice as new beta-solenoid AFP scaffolds. Indeed, Yu mutated a threonine ladder onto a protein from this class and the mutant displayed ice shaping and thermal hysteresis activity.[57] This novel AFP's thermal hysteresis activity was about an order of magnitude less than that of TmAFP, however, highlighting the possibility that some beta-solenoids may be more optimal AFP scaffolds than others.

This possibility is further supported by comparisons between AFPs and bacterial ice-nucleating proteins (INPs), which also have a beta-solenoid structure displaying a threonine ladder.[58–60] Recent computational studies have suggested that the ice-binding threonine ladder on sbwAFP deviates from that on an INP segment in terms of local water structure and dynamics[40] as well as ice nucleating ability.[61] Furthermore, like Yu's design, a truncated INP showed substantially reduced freezing point depression compared to hyperactive AFPs.[62] Plausible reasons for disparities in thermal hysteresis activity between different beta-solenoids with the same ice-binding residues include reduced binding due to altered geometry of the threonines, suboptimal scaffold shape or non-binding surface chemistry for resisting engulfment by ice, cooperative effects or additive structural mismatch dependent on the number of solenoid loops, and variations in the rigidity of the solenoid.

Here, we explore the first of those considerations: whether and how a threonine ladder's structural characteristics depend on the nature of the beta-solenoid scaffold. Liou et al. highlighted the remarkable regularity of the crystal structure of TmAFP, with its threonine hydroxyl groups exhibiting spacings nearly identical to those of water oxygens in the ice lattice.[26] We hypothesized that threonine ladders on distinct solenoid scaffolds may show differences in local structure that make them less optimal for ice binding, and that quantifying these differences may be useful for identifying beta-solenoids that are best suited for transformation into novel AFPs. Using pentapeptide repeat proteins as a model system, we

employed a combination of structure predictions and molecular dynamics (MD) simulations to assess how changes in the beta-solenoid scaffold impact the threonine ladder structure, as quantified by simple geometric features. Both analysis methods illustrated the threonine ladder's sensitivity to the concavity of the solenoid face it occupies, with the least concave solenoid faces providing the closest approximation to the IBS of TmAFP. By focusing predominantly on the causal details of the protein structure rather than on the behavior of nearby water molecules, we provide a bridge between the numerous existing studies of IBS hydration water properties and recent advances in protein structure prediction techniques — a bridge with practical implications for the design of new AFPs. We ultimately illustrate these practical implications by applying our findings to identify AFP-like beta-solenoid designs among sequences generated with the deep learning tool ProteinMPNN.[46]

Methods

Beta-solenoid variants

An initial model solenoid sequence was constructed by repeating the pentapeptide repeat consensus ADLSG[54,56] 24 times to form six square loops (Figure 1B). The inward-facing residues (X) at the center of each side of one 20-residue loop were substituted with V, F, or W or kept as L to create a non-exhaustive set of 40 distinct loops, each of which was repeated six times to make the threonine-free variants (labeled $X_1X_2X_3X_4$_DS). A threonine ladder was added to each by replacing the DXS on one face (side 2 counting from the N-terminus) with TXT in every loop to produce 40 more variants of the form $X_1X_2X_3X_4$_TT. The 20-residue loop sequences for all variants used are listed in Tables S1 and S2 of the Supporting Information. The average inward residue volume for a given sequence refers to the average volume of residues X_1, X_2, X_3, and X_4 based on the consensus volumes reported in Ref. 63.

Structure prediction and analysis

Except where otherwise indicated, our AlphaFold predictions refer to results from running ColabFold v1.5.5[64] in single-sequence mode with three recycles, without templates, and using the AlphaFold 2 ptm weights (all five models).[43] The structures were not relaxed. These settings were sufficient to obtain many highly confident solenoid predictions (Figures S2A and S2B of the Supporting Information). We further reasoned that running without multiple sequence alignments or templates may avoid biasing our analysis toward sequences more similar to those found in nature, as has previously been noted in the context of protein design pipelines.[48] Structure ranks refer to ranking each set of five structures by average pLDDT. Our AlphaFold 3[49] comparisons were run on AlphaFold Server with all default settings; mmCIF files from the server were converted to PDB format with the GEMMI web-based converter.[65]

We employed Biopython[66] and PYTRAJ,[67] the Python interface for CPPTRAJ,[68] for structure analysis. Note that we use atom names consistent with the Amber force field (see below) throughout our results (Figure S1 of the Supporting Information) and we refer to features by the names shown in Figure 1C. Angle and distance values for TmAFP are from PDB 1EZG chain A.[26] Threonines in predicted structures were considered to be in the intended rotameric state if their N-CA-CB-OG1 dihedral angle was $\geq$ -60° and $\leq$ -50°; the upper bound was changed to -45° for our ProteinMPNN sequences to account for slight scaffold-dependent differences.

MD simulations and analysis

All simulations were run with the CUDA-accelerated implementation of PMEMD in Amber22.[69–73] Chain A of PDB 1EZG (for TmAFP) and the top-ranked AlphaFold structures for the LLLL_TT, FFFF_TT, FFFF_DS, and WWWF_TT pentapeptide repeat variants were each solvated in a cubic water box using tLEaP from AmberTools,[69] with a 15 Å minimum buffer distance. The ff14SB force field[74] was used for the proteins, and water was represented

by the TIP4P-Ew model.[75] Each system underwent an energy minimization followed by heating in the NVT (constant number of particles, volume, and temperature) ensemble over 50 ps to reach the desired temperature (300 K or 242 K), with harmonic backbone restraints at both of these stages using a force constant of 10 kcal/mol·Å^2. Next for each system and each temperature we ran a 10-ns equilibration in the NPT (constant number of particles, pressure, and temperature) ensemble at 1 bar with weakened restraints (2 kcal/mol·Å^2). We then ran unbiased 100-ns NPT production simulations with no restraints, saving frames every 10 ps. Throughout the simulations we employed periodic boundary conditions, a cutoff of 12 Å for non-bonded interactions, a timestep of 2 fs, the SHAKE algorithm[76] to constrain lengths of bonds with hydrogen, the Langevin thermostat, and the Berendsen barostat (in NPT simulations). Example Amber inputs from our simulations are included in the Supporting Information.

We analyzed simulation trajectories using CPPTRAJ. For rotamer-filtered threonine OG1 distance distributions, only frames in which both threonines had a N-CA-CB-OG1 dihedral angle $\geq$ -75° and $\leq$ -50° were considered; these cutoffs were selected based on Figures S4A and S4B of the Supporting Information. We obtained the three-dimensional water oxygen density distributions in the space around the threonine ladders in the low-temperature simulations with CPPTRAJ's grid command using a grid spacing of 0.5 Å.

ProteinMPNN

Except for our tests of different sampling temperatures for the LLLL_TT starting structure, we ran ProteinMPNN with a temperature of 0.8. We used the v_48_020 model, we excluded cysteines, and we fixed the two rows of threonines on our selected IBS face for each case.

Structure and data visualizations

All structure visualizations were created with UCSF Chimera,[77] including images of the water oxygen density distributions produced with Chimera's Volume Viewer tool. Python

and Matplotlib[78] were used for all plots; distribution plots were made with the Seaborn library[79] using kernel density estimation. We produced sequence logos with WebLogo.[80]

Results

Structure predictions for variations of a model beta-solenoid

We constructed a highly regular initial model beta-solenoid by repeating the pentapeptide repeat consensus pattern ADLSG 24 times to form six four-sided loops. From this starting point, we diversified the solenoid scaffold by creating 40 variants differing in the volume of the inward-facing hydrophobic residues in the center of each face of the repeated loop, and for each of these variants we made a version with the outward-facing residues on one side changed to threonines, converting the DXS pattern to a TXT motif in each loop. Each variant is henceforth referred to as $X_1X_2X_3X_4$_Z_1Z_2, where X_i is the central inward residue on side i of the repeated loop and Z_1/Z_2 are the outward-facing residues on side 2 (the second side counting from the N-terminus) (Figure 1B). According to this system, the original consensus sequence consisting of 24 repeats of ADLSG is labeled LLLL_DS. We used the ColabFold implementation of AlphaFold 2 to predict structures of the resulting 80 sequences (40 with a threonine ladder and 40 without, with loop sequences listed in Tables S1 and S2 of the Supporting Information).

The majority of the predicted structures had high pLDDT values and low alpha-carbon RMSD with respect to the highest-ranked predicted structure of LLLL_DS, suggesting that the pentapeptide repeat protein beta-solenoid structure may be fairly tolerant of various hydrophobes in the inward-facing residue positions, and/or that AlphaFold readily predicts this structure regardless of deviations from natural sequences in this family. Lower pLDDT and greater structural variation occurred in a subset of cases involving particularly high and low inward residue volumes (mainly tryptophan or valine) (Figures S2A and S2B of the Supporting Information). Only highly confident beta-solenoid structures were considered for

further analysis, with average pLDDT greater than 90 and CA RMSD to LLLL_DS (rank 1) less than 2.0 Å. Out of the 247 predicted structures meeting those criteria, nine exhibited topological deviations involving corner alanines flipped outward (Figure S2C of the Supporting Information), disrupting the typical inward-outward-inward-outward-outward pattern; these cases were also excluded from subsequent analysis.

Treating the average volume of the central inward-facing residues as our independent variable, we defined a set of four simple geometric features that could readily be calculated from the predicted structures to assess the impact of differences in the inward residues. These features are illustrated in Figure 1C and are denoted using atom names depicted in Figure S1 of the Supporting Information. Terminal loops were not included in the calculation of these features because we expected greater structural variability near the termini. As AlphaFold can sometimes be robust to minor sequence changes and thus imperfect for predicting the effects of mutations,[81] we first sought to confirm that our AlphaFold structures showed a physically reasonable response to the differences in inward residue bulk. We reasoned that the square beta-solenoid profile may progressively bulge as the inward residues increase in size. Consistent with this expectation, the distance between the alpha carbon atoms of the eigth and 18th residues in each loop (the central inward residues of sides 2 and 4) generally increased as the average inward residue volume increased both in the variants with threonine ladders and in those without (Figure 2A). This feature, henceforth called the (i + 8)-(i + 18) CA distance (with i representing the number of residues before the start of the loop in question), should not be directly relevant for ice binding but demonstrated AlphaFold's ability to show differences in beta-solenoids with identical topologies.

Next we assessed structural features specific to the putative IBS (or the analogous DXS face in the threonine-free variants). We supposed that the inward residues might influence the concavity of the beta-solenoid's faces, as quantified for our selected IBS by the side 2 CB-CA-CB angle, which in turn could affect the spacings between the threonines' hydroxyl oxygen (OG1) atoms. For the variants with threonine ladders, the AlphaFold structures showed the

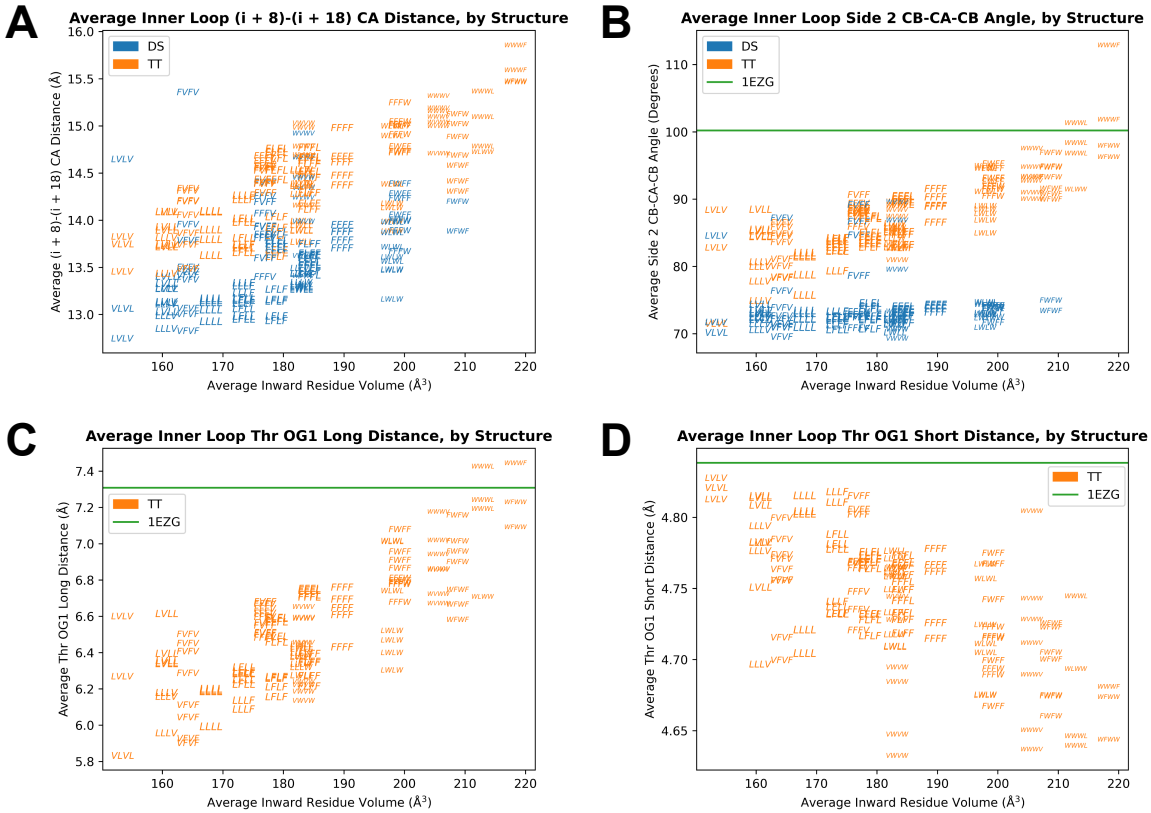

Figure 2: Geometric features from AlphaFold structures with respect to the average inward residue volume for the pentapeptide repeat variants, including (A) the (i + 8)-(i + 18) CA distance, (B) the side 2 CB-CA-CB angle, (C) the threonine OG1 long distance, and (D) the threonine OG1 short distance. Each data point, representing an average over the four inner (non-terminal) loops in one of the five predicted structures for a given sequence, is denoted by the inward residues of the variant's four faces ($X_1X_2X_3X_4$), with the Z_1/Z_2 residues indicated by the color (blue for threonine-free variants and orange for those with threonine ladders). Only structures with average pLDDT greater than 90 and CA RMSD to LLLL_DS rank 1 less than 2.0 Å and without topological deviations are included in (A) through (D), and only structures which also had all inner-loop threonines in the expected rotameric state are included in (C) and (D). In (B) through (D) values from TmAFP (PDB 1EZG chain A) are shown by a green line for comparison.

trend we expected: The side 2 CB-CA-CB angle increased for larger inward residue volumes, indicating that the threonine ladder face became less concave (Figure 2B). However, this trend was absent for the corresponding DXS face of the variants without threonine ladders. We suspect that hydrogen bonding between the aspartate and serine residues might make the backbone and side chain geometry of these variants relatively indifferent to the inward residues, unlike threonines which appeared more sensitive to changes in the scaffold.

Furthermore, the distance between the hydroxyl oxygens of adjacent threonines in the same loop (henceforth the OG1 "long distance") showed a positive correlation with inward residue volume (Figure 2C). The "short distance" (between adjacent threonine oxygens in consecutive loops) showed a negative correlation but over a much narrower range of values (Figure 2D). Only structures with threonines in the same rotameric state as those in TmAFP's crystal structure were considered in Figures 2C and 2D; most structures met this criterium, exhibiting N-CA-CB-OG1 dihedral angles between -60° and -50° (Figure S2D of the Supporting Information). For both the side 2 angle and the OG1 long distance, the bulkiest inward residues yielded values closest to the crystal structure of TmAFP, which exhibits OG1 long distances much nearer to the longer oxygen spacings in the primary prism (7.35 Å) and basal (7.83 Å) planes[26] of ice than do the solenoids at the low end of the inward residue volume distribution. The OG1 short distances on the other hand were entirely within the range between the data point from TmAFP's crystal structure and the ice lattice spacing of 4.52 Å.

Assessment of structural trends with MD simulations

To determine whether the trends from AlphaFold's static structure predictions would be upheld by physics-based methods incorporating dynamics, we selected four variants for analysis with MD simulations under ambient conditions. We chose the variants LLLL_TT, FFFF_TT, and WWWF_TT to encompass cases with low, intermediate, and high inward residue volume, respectively, as well as FFFF_DS to include a direct comparison to a variant without a TXT face. TmAFP was also simulated as a reference. Importantly, we note that our pentapeptide repeat protein simulations, which were prepared using AlphaFold structures for initial coordinates, do not constitute independent structure predictions but rather provide an evaluation of the stability of our AlphaFold structures and indicate whether the relatively subtle differences in the geometric features are preserved as the structures fluctuate.

At 300 K, all of the pentapeptide repeat protein variants were largely stable for the 100-ns

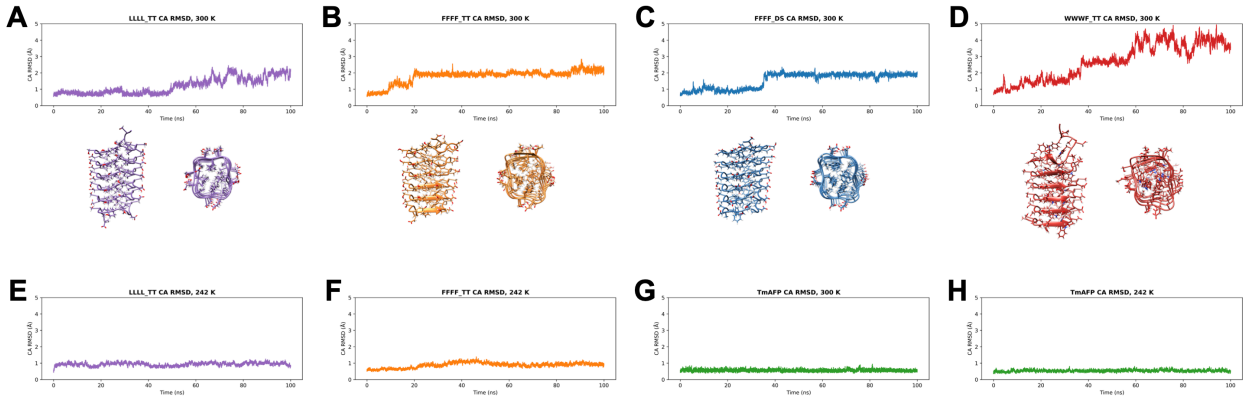

Figure 3: Alpha-carbon RMSD with respect to the initial structure over a 100-ns simulation for (A) LLLL_TT at 300 K, (B) FFFF_TT at 300 K, (C) FFFF_DS at 300 K, (D) WWWF_TT at 300 K, (E) LLLL_TT at 242 K, (F) FFFF_TT at 242 K, (G) TmAFP at 300 K, and (H) TmAFP at 242 K. Below the RMSD plots in each of (A) through (D) are two views of the final structure from the end of the respective simulation at 300 K.

duration of the simulation except for WWWF_TT, which showed high CA RMSD values (up to approximately 5 Å) and appeared to be unraveling at the C-terminal end (Figures 3A-D). WWWF_TT's inward residues are especially large and therefore tightly packed, making its instability unsurprising. The AlphaFold results had already hinted at this possibility: Only two of WWWF_TT's five predicted structures had passed our filters for analysis; the other three all had the aforementioned topological deviation illustrated in Figure S2C of the Supporting Information, and two of them also had an average pLDDT less than 90. In contrast, all five AlphaFold structures for each of LLLL_TT, FFFF_TT, and FFFF_DS had RMSD less than 1.0 Å with respect to LLLL_DS rank 1, and the lowest-ranked structures for those variants had average pLDDT values of 94.4, 96.6, and 95.4, respectively.

Because of its apparent instability, WWWF_TT was not included when we subsequently simulated the other two threonine ladder-bearing variants, along with TmAFP, at 242 K, a temperature near the melting point of the TIP4P-Ew water model.[82,83] LLLL_TT and FFFF_TT remained stable at 242 K (Figures 3E and 3F), and TmAFP showed very little variability at either temperature (Figures 3G and 3H), emphasizing this protein's notable rigidity, as others have described previously.[35,84] We observed for all of the pentapeptide

repeat variant simulations at both temperatures that the CA RMSD for only the inner four loops stayed lower than the overall CA RMSD (Figure S3 of the Supporting Information), suggesting that the majority of the structural deviations came from variability in the terminal loops. The relative stability of the inner loops, even in WWWF_TT, confirms that they are suitable for analysis to determine whether the simulations reinforce the AlphaFold results, and also to investigate whether LLLL_TT and FFFF_TT exhibit IBS-like behavior at low temperature.

While showing differences in the values of some geometric features, the simulations at 300 K maintained the relationships between solenoid variants with different inward residue volumes, as well as the contrast between analogous variants with and without a threonine ladder, that were originally observed in our AlphaFold structures. Compared to these simulations, AlphaFold appeared to underestimate the (i + 8)-(i + 18) CA distance for FFFF_DS, FFFF_TT, and WWWF_TT but not LLLL_TT (Figure 4A). However, like in the predicted structures, this distance increased with increasing inward residue volume from LLLL_TT to FFFF_TT to WWWF_TT, and was smaller for FFFF_DS than for FFFF_TT. The latter outcome is consistent with the threonine-free variants generally falling below the threonine ladder variants in Figure 2A and further suggests that the threonines themselves may slightly reduce the concavity of the face they occupy compared to the aspartate/serine combination on the same scaffold. The simulated threonine ladder CB-CA-CB angle distributions also mirrored the predicted dependence on inward residue volume, with WWWF_TT nearest to TmAFP's distribution, LLLL_TT farthest from TmAFP, and FFFF_TT intermediate (Figure 4B). Interestingly, LLLL_TT's contrast to TmAFP's IBS in concavity appeared somewhat more drastic in the simulation than in the AlphaFold prediction. FFFF_DS presented smaller angle values than FFFF_TT, again maintaining the trend from AlphaFold.

Analyzing the threonine OG1 distances from the simulations necessitated accounting for variability in the rotameric states of the threonines over time. Consistent with experimental findings[85,86] as well as previous computational modeling,[36] in our simulations TmAFP's

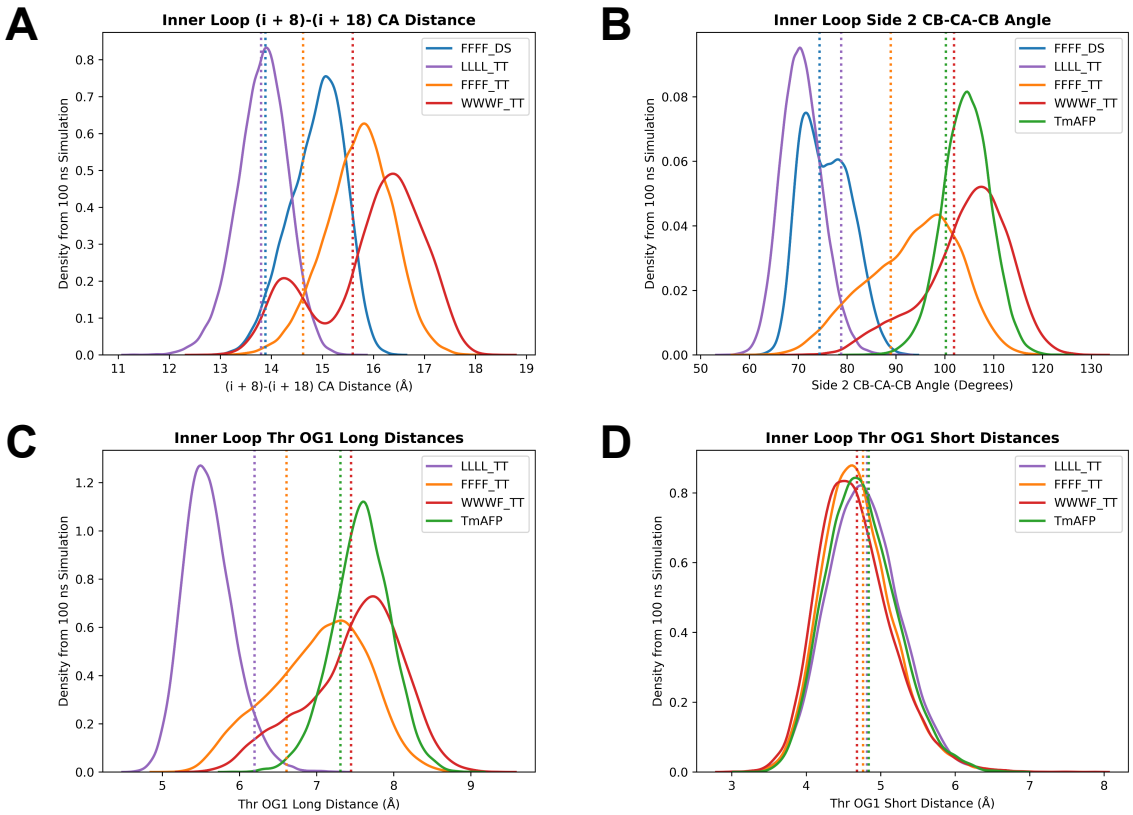

Figure 4: Simulation results at 300 K, including distributions of (A) (i + 8)-(i + 18) CA distances, (B) side 2 CB-CA-CB angles, (C) threonine OG1 long distances, and (D) threonine OG1 short distances. The OG1 distances are filtered based on the threonines' rotameric states; the unfiltered distributions at 300 K are shown in Figures S4C and S4D of the Supporting Information. Terminal loops are not included in these distributions. In all panels, vertical dashed lines represent the values from the rank 1 AlphaFold structures (or PDB 1EZG chain A for TmAFP).

threonines predominantly occupied the same rotameric conformation observed in the crystal structure (Figures S4A and S4B of the Supporting Information).[26] However, the threonines in TmAFP and our pentapeptide repeat variants showed a sufficient degree of rotational variability, particularly at 300 K, to require filtering simulation frames based on threonine rotamers to permit a more direct comparison to OG1 distances from our AlphaFold structures and also to focus on the state of the threonine ladders believed to be optimal for ice binding. As it has been suggested that the rotations of the threonine side chains may differ between distinct protein force fields,[87] we reasoned that restricting our distance analysis to the relevant state provided a simple way to reduce the force field dependence of our conclusions.

Figures 4C and 4D present the threonine OG1 long and short distance distributions at 300 K after this rotamer filtering. WWWF_TT and to a slightly lesser degree FFFF_TT substantially overlapped TmAFP's OG1 long distance distribution, while the simulation reinforced LLLL_TT's contrast (Figure 4C). Like in the predicted structures, the threonine OG1 short distances all displayed very similar distributions in these simulations (Figure 4D). The OG1 distance distributions without rotamer filtering are included in Figure S4 of the Supporting Information; they showed the same trends with the exception that the filtering was critical to disambiguate a bimodal distribution in TmAFP's OG1 long distance (Figure S4C of the Supporting Information).

Our simulations at 242 K confirmed that the same relationships between the structural features of LLLL_TT, FFFF_TT, and TmAFP persisted at a functionally relevant temperature (relative to the water model). At this lower temperature, LLLL_TT again exhibited a smaller (i + 8)-(i + 18) CA distance than FFFF_TT (Figure 5A), and FFFF_TT continued to be closer to TmAFP than LLLL_TT was in side 2 CB-CA-CB angle and threonine OG1 long distance (Figures 5B and 5C). Like at 300 K, the OG1 short distances showed little difference between the proteins (Figure 5D). The OG1 distance distributions without rotamer filtering produced the same relationships with more variability (Figures S4E and S4F of the Supporting Information).

Interestingly, at 242 K FFFF_TT's (i + 8)-(i + 18) CA distance possessed a lower shoulder, a detail mirrored in the shapes of this variant's CB-CA-CB angle and threonine OG1 long distance distributions (Figure 5A-C). We supposed that one or more changes between two states of the solenoid's profile might have impacted the IBS features. To explore this possibility, we assessed the (i + 8)-(i + 18) CA distance and its perpendicular analog, the (i + 3)-(i + 13) CA distance, with respect to time (Figures S5A and S5B of the Supporting Information). Slightly more than 20 ns into the simulation, the former distance increased while the latter decreased: The originally square profile had shifted toward a more rectangular state. At the same point in time, the side 2 (TXT) CB-CA-CB angle increased

(Figure S5C of the Supporting Information). Meanwhile the opposing side 4 (DXS) CB-CA-CB angle (Figure S5D of the Supporting Information) showed no distinguishable response to the elongation of the solenoid's profile in one dimension. These observations suggest that the geometry of a threonine ladder is more tightly coupled to the shape of its solenoid scaffold than is the geometry of a DXS face, corroborating the distinction that appeared in our CB-CA-CB angle data from AlphaFold, with the threonine-free variants lacking the dependence on inward residue volume (Figure 2B).

Our use of explicit water in the simulations permitted analysis of ordered waters near the IBS. Prior studies have established the presence of ordered waters between the threonine rows in several AFPs;[26,31,33,35,36,38,40,41] we used our low-temperature simulations to determine whether the LLLL_TT and FFFF_TT variants possessed these channel waters.

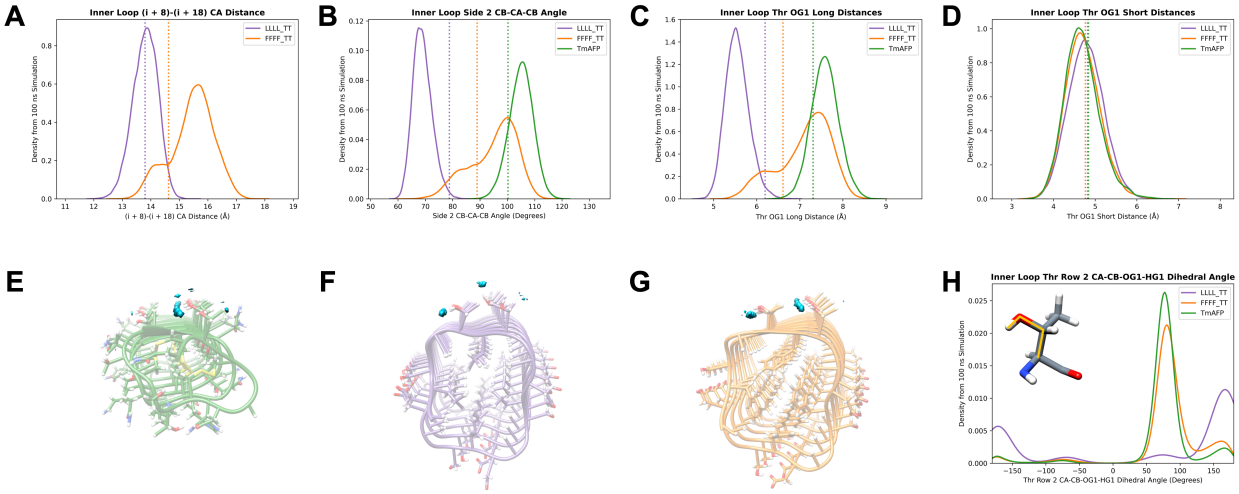

Figure 5: Simulation results at 242 K, including distributions of (A) (i + 8)-(i + 18) CA distances, (B) side 2 CB-CA-CB angles, (C) threonine OG1 long distances, and (D) threonine OG1 short distances, again only for inner (non-terminal) loops and with values from the initial structures indicated with vertical dashed lines. The OG1 distances are filtered based on the threonines' rotameric states; the unfiltered distributions at 242 K are shown in Figures S4E and S4F of the Supporting Information. (E) through (G) show the locations of peaks in water oxygen density around the threonine ladders alongside average structures of (E) TmAFP, (F) LLLL_TT, and (G) FFFF_TT, with a threshold of 5%. Note that the average coordinates do not necessarily represent realistic individual conformations and some side chains therefore appear distorted. (H) Distributions of the CA-CB-OG1-HG1 dihedral angles (inset) from inner loops at 242 K.

Like TmAFP, FFFF_TT displayed the expected peaks in water oxygen density between the threonines (based on an isosurface threshold identifying positions containing a water oxygen for at least 5% of the production frames), whereas LLLL_TT was missing these channel waters (Figures 5E-G). Even at a lower threshold of 1%, these peaks were absent between LLLL_TT's threonines (Figure S6 of the Supporting Information).

To visualize the positions of the water oxygen density peaks relative to the IBS we had created average structures of the proteins. We noticed from the average structures that LLLL_TT's second row of threonines (on the right-hand side) appeared to have the hydroxyl hydrogens pointing away from the beta-solenoid on average, unlike TmAFP and FFFF_TT which had these hydrogens pointing down toward the channel waters (Figures 5E-G). To examine this difference in more detail, we checked the CA-CB-OG1-HG1 dihedral angle distributions for the second-row threonines (excluding those in terminal loops) from all three simulations at 242 K. As the average structures had indicated, LLLL_TT's threonine hydroxyl groups displayed a clear divergence in orientation from those of TmAFP and FFFF_TT (Figure 5H). We postulate that the greater concavity of LLLL_TT's TXT face results in insufficient spacing between the threonine rows to accommodate channel waters and thus drives the second row's hydroxyl groups to donate hydrogen bonds to water oxygens above the threonine ladder (visible in Figure 5F) rather than within its ranks. LLLL_TT's contrast to the other two proteins was further emphasized by the different orientation of the carbonyl group of the X residues' backbone in the TXT motifs, making its carbonyl oxygens unavailable for hydrogen bonding with channel waters (Figure S7 of the Supporting Information).

Demonstration of AlphaFold's potential utility for designing AFP-like beta-solenoids

Both AlphaFold and MD simulations supported our hypothesis that the structural details of a threonine ladder can be influenced by the beta-solenoid scaffold. While the simula-

tions were essential to analyze additional factors such as the ordered water locations and the proteins' backbone and side chain dynamics, AlphaFold indicated distinctions in the IBS geometric features very efficiently, suggesting the possibility of a multi-tiered filtering process for designed beta-solenoid sequence candidates that could begin with AlphaFold for high-throughput preliminary screening. Screening of generated sequences with AlphaFold is common in computational protein design campaigns;[48,88] our results imply that such a screening in an AFP design workflow can go beyond overall structure checks to also provide reasonable initial indications of IBS suitability, at least in the case of a threonine ladder IBS. We therefore concluded our study with a demonstration of how AlphaFold can be used to help identify promising novel AFP sequences, summarized in Figure 6A.

With our initial creation of variants from the pentapeptide repeat consensus ADLSG, we already established that beta-solenoid variants can be derived from consensus sequences. We supplemented our demonstration by exploring an alternative means of constructing potential AFP scaffolds based on single loops of natural beta-solenoids. Assisted by Kajava and Steven's thorough inventory of beta-solenoid proteins,[89] we browsed the Protein Data Bank[90] and selected 4OJ5,[91] 4MZU,[92] and 6RIB[93] as starting points. These structures represent a putative bacteriophage tailspike protein, a bacterial biosynthetic enzyme, and a bacterial cytoskeleton component, respectively. From each structure we identified the sequence of one arbitrarily chosen loop of the solenoid; a second, different loop was taken from 4MZU for greater variety. Similar to our original strategy of repeating ADLSG to form a six-loop solenoid, we repeated each loop sequence from the PDB structures six times to produce initial solenoid sequences.

We predicted five structures of each initial solenoid with AlphaFold. The solenoid derived from 4OJ5 had long faces that could be suitable for hosting more than two rows of threonines (Figure S8 of the Supporting Information); while less relevant to the present investigation centered on the two-row threonine IBS, this scaffold may yet hold promise for future design of AFPs/IBPs with larger ice-binding faces. This solenoid was not subjected to further

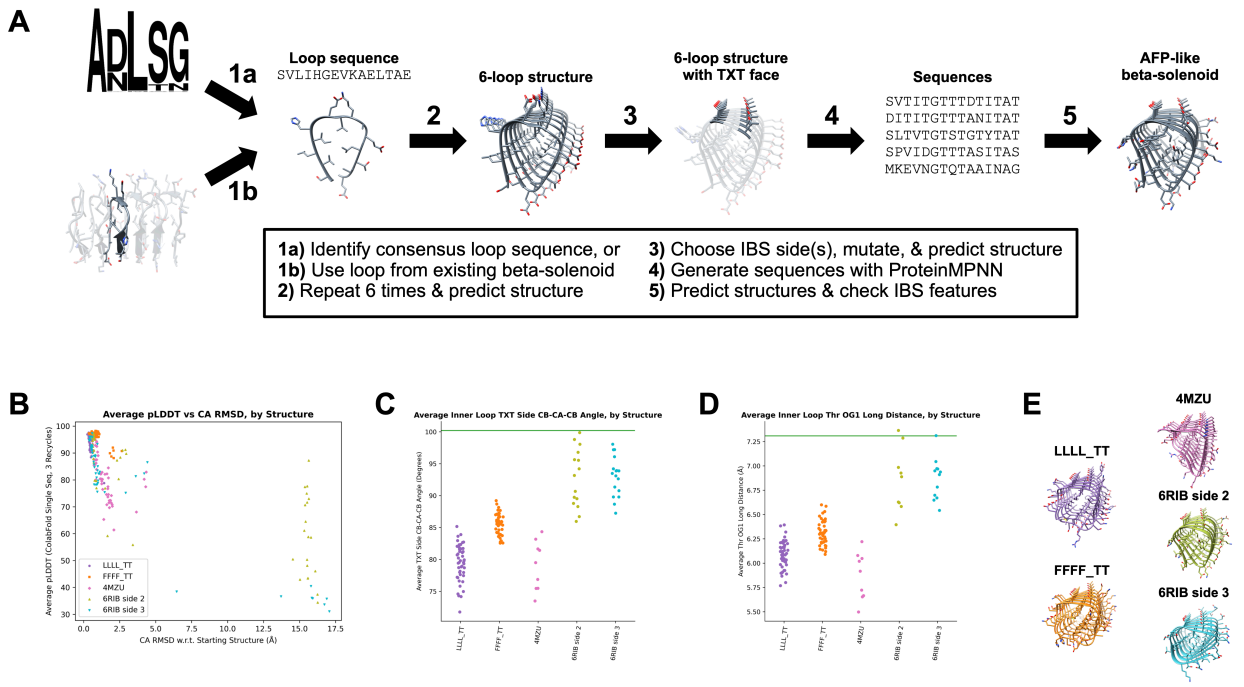

Figure 6: (A) Overview of our strategy to generate beta-solenoid sequences and screen them for favorable IBS features. (B) Average pLDDT versus CA RMSD (with respect to the corresponding starting structure) for each AlphaFold 2 structure for each sequence generated with ProteinMPNN. (C) Average TXT side CB-CA-CB angle and (D) average threonine OG1 long distance from non-terminal loops for each predicted structure with pLDDT greater than 90 and CA RMSD less than 2.0 Å, with (D) displaying only those that also had all inner-loop threonines in the expected rotameric state. The horizontal green lines in (C) and (D) reoresent values from TmAFP (PDB 1EZG chain A). (E) Rank 1 AlphaFold structures for the most promising sequence from each starting point, as determined by selecting the candidate with all five predicted structures passing our pLDDT and RMSD filters that had the largest average CB-CA-CB angle. The corresponding sequences are listed in Table S3 of the Supporting Information.

engineering. One of the two sequences from 4MZU was also dropped on account of low average pLDDT (58.0 for the top-ranked prediction). Interestingly, the 6RIB loop gave five structures with at least relatively high average pLDDT (ranging from 80.4 to 95.6) but only three were right-handed beta-solenoids; the rank 3 structure was a single alpha helix and the rank 5 structure was a left-handed beta-solenoid. As the other 4MZU loop and the 6RIB loop had both yielded confident solenoid structures (albeit with variability), we used their highest-ranked predicted structures to visually select faces with two rows of outward-facing residues to bear the threonine ladder as a potential IBS: We proceeded with one face for

the solenoid from 4MZU and two different faces for the solenoid from 6RIB (labeled side 2 and side 3). We mutated the sequences accordingly and predicted structures again. At this point we had produced three perfectly repetitive, highly regular beta-solenoids with threonine ladders, analogous to the LLLL_TT, FFFF_TT, etc. variants we had developed from the consensus sequence.

To diversify these repetitive beta-solenoids and develop potentially more realistic sequences, we next used the inverse folding model ProteinMPNN to generate sequence candidates based on the rank 1 AlphaFold structures of the PDB-derived solenoids (from 4MZU and 6RIB side 2 and side 3) and the consensus-derived LLLL_TT and FFFF_TT solenoids. Initial tests with LLLL_TT revealed that a high sampling temperature is necessary to achieve substantial variability in generated beta-solenoid sequences (Figure S9 of the Supporting Information). Thus with a sampling temperature of 0.8, we generated 10 alternative sequences for each of the five structures, keeping the IBS threonines fixed. AlphaFold structures were predicted for all of the sequences. While a small number of sequences per structure was sufficient for the purpose of this demonstration, the computational efficiency of ProteinMPNN and AlphaFold makes this approach readily applicable to larger batches of designs.

Even at this high sampling temperature, ProteinMPNN produced many sequences confidently predicted to form beta-solenoids. Out of 250 structures (five predicted structures for each of 10 sequences for each of five starting structures), 132 had average pLDDT greater than 90 and showed CA RMSD less than 2.0 Å with respect to their starting structure. Those 132 structures represented 30 different sequences, 21 of which had all five predicted structures passing the pLDDT and RMSD cutoffs (Table 1). Only 6RIB side 2 yielded entirely distinct structures with moderate confidence (Figure 6B).

We compared the TXT face's CB-CA-CB angle for all passing structures and the threonine OG1 long distance for all structures with inner-loop threonines in the proper rotameric state (Figures 6C and 6D). Like in our original AlphaFold results and simulations, these features remained correlated, with each showing the same relationships between the five

Table 1: AlphaFold Results for ProteinMPNN Sequences.

	# Seqs with ≥ 1 Passing Structure	# Seqs with 5 Passing Structures
LLLL_TT	10	8
FFFF_TT	9	8
4MZU	2	1
6RIB side 2	5	2
6RIB side 3	4	2

groups of designs. As expected, between the LLLL_TT and FFFF_TT starting structures, FFFF_TT yielded designs with angle and distance values closer to TmAFP. The designs based on 4MZU exhibited small angles and distances similar to those from LLLL_TT, indicating that these two scaffold sets possessed the most concave TXT faces. The sequences produced from 6RIB (both side 2 and side 3) came nearest to TmAFP's angle and distance values and thus closest to the aforementioned ice lattice spacings, suggesting that this scaffold may be the most optimal for AFP design out of those examined (in terms of IBS geometry) and even offers multiple options for the location of the IBS.

Having previously observed in our simulations the instability of a variant (WWWF_TT) that had variable AlphaFold results, we reasoned that the ProteinMPNN sequences with the most consistent and confident predicted structures may have the greatest likelihood of stability. For each group of designs, we therefore identified the most promising sequence as the one with all five AlphaFold structures passing our pLDDT and RMSD filters that had the largest IBS CB-CA-CB angle (averaged over all five structures). Figure 6E displays the top-ranked AlphaFold structure for each of these leading candidates; the sequences are provided in Table S3 of the Supporting Information. In this way we have applied our findings from the pentapeptide repeat variants to efficiently assess the viability of novel beta-solenoid sequence designs—a step toward new hyperactive AFPs.

Discussion

The threonine ladders found on a subset of AFPs are perhaps nature's most elegant solution to what has been described as the greatest recognition challenge in biology — the differentiation between water's solid and liquid phases.[94] Two rows of threonine residues constitute a minimalist IBS that is sufficient for ice recrystallization inhibition at submicromolar concentrations[95] as well as high thermal hysteresis activity,[28,29] making this type of IBS highly promising for use in designing novel AFPs. By demonstrating that the structure of a threonine ladder IBS can be significantly influenced by the beta-solenoid scaffold, we attempted to augment the growing body of knowledge of IBS function that will inform design efforts in this area.

Our findings not only reinforce past comparisons but also have both retrospective and prospective implications for AFP design. Differences in the concavity of the solenoid faces might at least partially explain disparities in the thermal hysteresis activity[62] and computationally studied water ordering[40,61] between insect AFPs and INP segments. Additionally, the comparisons in the present study indicate a possible reason for the low thermal hysteresis activity of the pentapeptide repeat protein previously transformed into a new AFP by Yu.[57] The cyanobacterial pentapeptide repeat protein used (PDB 2J8K) had the LLLL pattern of inward-facing hydrophobes throughout all of its loops with the exception of a single phenylalanine near the N-terminal cap.[96] Based on the analysis of our LLLL_TT variant, this solenoid's installed TXT face may have been overly concave, with small OG1 long distances, and possibly unable to accommodate channel waters as well as a natural AFP would. Intriguingly, the ice shaping that was nevertheless observed for Yu's mutated protein hints that even an apparently suboptimal threonine ladder face may not entirely preclude ice binding. Our results suggest that the activity of this novel AFP can potentially be improved by mutating some or all of its inward-facing leucines to phenylalanines, or by starting from a pentapeptide repeat protein with higher average inward residue volume in the first place, such as MfpA from *Mycobacterium tuberculosis* which has more internal phenylalanines.[55]

Either option may confer a more AFP-like threonine ladder IBS.

Looking forward, we anticipate state-of-the-art methods for protein design to open up many exciting possibilities for IBP design. For instance, de Haas et al. recently reported intriguing results from the application of computational design tools to the creation of alpha-helical IBPs.[97] As the beta-solenoid fold is capable of producing relatively flat, parallel beta-sheet faces with a high degree of regularity, methods for designing beta-solenoids (e.g., Refs. 56,98,99) may be central to the further development of novel ice binders. We have confirmed the need to carefully consider how different solenoid scaffolds can affect IBS geometry, and in the process of demonstrating how this information can be applied to sequence candidate screening, we illustrated one potential way to generate new beta-solenoid sequences: repeating an initial loop sequence to obtain a starting structure for inverse folding. As we showed in Figure 6, this strategy can produce sequences confidently predicted by AlphaFold to fold into regular solenoids with TXT faces exhibiting comparable flatness to TmAFP. Furthermore, the applications of methods for beta-solenoid design reach beyond ice modulation into the area of nanomaterials, such as nanowires,[100,101] cages,[56,102] solid coatings,[103] semiconductor templates,[99] and protein-based porous or catalytic frameworks.[56,104–107]

More steps may be necessary to complete our AFP designs. Without capping structures or terminal irregularities, beta-solenoid AFPs can assemble into amyloid fibrils.[100,101] While forming an extended IBS through self-assembly may be desirable for ice nucleation activity,[108–111] designs that do not assemble will be more similar to natural AFPs. Thus we would consider modifying our ProteinMPNN designs by attaching capping groups based on natural solenoids,[56] diffusing caps with RFdiffusion,[48] or simply mutating select residues in both terminal loops to like-charged amino acids.

We chose to focus our investigation on features related to the flatness or concavity of the beta-solenoid face hosting a threonine ladder, but as we acknowledged, this is only one of many factors that may influence an AFP's ice-binding capacity and activity. We observed in our simulations for instance that TmAFP displayed exceptional backbone rigidity (Fig-

ures 3G and 3H), as has been noted previously,[35,84] which likely contributes to its function; other solenoid scaffolds may be more flexible. Qualitatively, we also noticed differences in our solenoids' degree of twist (visible in the structures in Figures 5F and 5G). Twisting can reduce a threonine ladder's complementarity to the ice surface. Aside from the IBS itself, the impact of an AFP's shape and non-IBS surface chemistry on its activity is only beginning to be understood.[112] Our strategy for generating beta-solenoid sequences offers a path to new comparisons that may help to address this uncertainty. Importantly, the expanding toolkit for protein design also presents new opportunities to isolate the effects of specific features, as de Haas et al. illustrated by precisely constraining the twist in their alpha-helical IBPs.[97]

While the consistency between our two computational approaches appears to strengthen our claims about the distinctions between beta-solenoid scaffolds, it is essential to note the limitations of both methods. For example, the residue flips we observed variably in a subset of our AlphaFold structures, as illustrated in Figure S2C of the Supporting Information, indicate that AlphaFold may easily make local topological errors in beta-solenoid structures even while maintaining high confidence. This type of topological deviation was previously noted when an AlphaFold structure of an INP[60] was compared to an earlier homology-based model;[59] Pal et al. recently demonstrated that the flipped scaffold residue differing between the two structures altered the INP's ice-nucleating ability in simulations, with the AlphaFold structure appearing more favorable.[61] Additionally, the inconsistent handedness we observed in the lowest-ranked structure for the initial six-loop sequence from 6RIB suggests that AlphaFold might struggle to distinguish right-handed from left-handed beta-solenoids. Both cases are represented among natural hyperactive AFPs,[26,113] thus one handedness may not be strongly preferable in AFP design, but predicting handedness incorrectly may still affect the success of the design process.

Beyond these structural details that may be predicted imperfectly, it has been proposed that AlphaFold (particularly AlphaFold 2) can frequently predict confident but unrealistic beta-solenoids for meaningless random sequence repeats,[114] compelling us to examine how

this potential capacity to hallucinate solenoids impacts each facet of our results and conclusions. Our initial 40 pentapeptide repeat protein variants were derived from a consensus sequence for a family of natural proteins with multiple representatives in the Protein Data Bank (e.g., PDB 2BM4[55] and 2J8K[96]), thus the predominance of quadrilateral, right-handed beta-solenoids predicted for our sequences is expected and we know this fold can exist for sequences relatively similar to ours. In addition, design efforts have already established the resilience of this fold to redesign beyond the natural sequence space.[56] That said, the solenoid sequences we constructed were unnaturally repetitive and some contained inward-facing residues valine or tryptophan that are not well represented at those positions in natural pentapeptide repeat proteins,[54,56] making it highly plausible that some of our predicted solenoids are fictitious. We observed the most structural variability at the high and low extremes of the inward residue volume range (Figure S2A of the Supporting Information), consistent with the inward residue options of intermediate size (leucine and phenylalanine) being those commonly found in natural sequences in the pentapeptide repeat family,[54] hinting that at least in aggregate AlphaFold favored the more evolutionarily realistic sequences, even without using multiple sequence alignments.

Ultimately, our conclusions about the effects of a TXT face's concavity are not dependent on our model beta-solenoids' realism. Our goal in creating the pentapeptide repeat variants was to analyze potential distinctions between threonine ladders on scaffolds that differed in a specific, controllable way. Inward residue volume, as we defined it in Figure 1C, served as an effective independent variable only as long as the same fold was analyzed in every case; any topological variations like that in Figure S2C of the Supporting Information could decouple this feature from the structure of the face hosting the threonine ladder. It is for this reason that we filtered our predicted structures by CA RMSD before analysis, excluded structures with flipped alanines, and confirmed the low CA RMSD of the four inner loops in our simulations.

On the other hand, AlphaFold's propensity to predict beta-solenoids has pronounced

implications for the design of new AFPs. On the positive side, this propensity makes it exceptionally easy to generate new solenoid designs *in silico*, as we did per Figure 6A. Hallucination of false structures is an acceptable and even useful component of the design process at step 2, where a solenoid structure is created for later use in inverse folding, analogous for instance to the backbone generation element of design pipelines featuring RFdiffusion followed by ProteinMPNN.[48] It is at step 5 in our illustrated workflow where unrealistic solenoid predictions become problematic: Screening designed sequences for an intended solenoid fold with AlphaFold may be prone to false positives, necessitating additional evaluation of the designs with different computational tools and eventually with experimental assessment of multiple candidates. Despite the possibility of false positives, AlphaFold 2 remains a valuable first step for screening large batches of sequence designs as it is a computationally efficient means of identifying candidates worthy of further attention and, as we have shown, can suggest both potential instability and subtle differences in IBS geometry. As protein structure prediction methods continue to emerge and improve,[49,50,52] future studies will likely explore how they compare to AlphaFold 2 in their capacity to meaningfully predict beta-solenoid structures. Pratt et al. already noted AlphaFold 3's improvement over AlphaFold 2 in this regard.[114] AlphaFold 3 consistently predicted beta-solenoids for our top ProteinMPNN sequences (those in Figure 6E and in Table S3 of the Supporting Information), with little difference from the starting backbone for all except that from 4MZU, which flipped handedness (Figure S10 of the Supporting Information).

MD simulations can also be employed in subsequent filtering and analysis of beta-solenoid AFP designs that appear promising based on structure predictions. However, simulations come with their own set of limitations. Our 100-ns simulations may not have been long enough to reveal instability in all cases, allowing structures to appear stable when they may actually be only metastable. Inaccuracies in common protein force fields and water models can further limit the predictive ability of simulations, and different force fields and water models can yield entirely different conclusions about structural and dynamical characteris-

tics.[87,115–120] We controlled for this impact on threonine rotamer variability but not in other contexts. For instance, while our low-temperature simulation of TmAFP showed its second-row threonine hydroxyl hydrogens pointing down toward the channel waters (Figures 5E and 5H), in a recent publication Zhang et al. opted for different protein and water parameters and displayed simulation snapshots with the hydroxyl hydrogens pointing up, similar to our LLLL_TT case (Figure 5F), but with the channel waters still present.[41] More accurate models for simulating proteins in water will be necessary to resolve this ambiguity. Nevertheless, our simulations provided a physics-based corroboration of the trends that emerged in our structure predictions and indicated how ordered waters may fit into these trends.

Conclusions

In the present work we set out to provide new details to inform the future design of beta-solenoid AFPs. We conclude that the geometry of a threonine ladder IBS is sensitive to the beta-solenoid scaffold upon which it is arrayed, and that subtle differences between scaffolds with the same overall topology can be sufficient to impact the threonines' ability to match the ice lattice and even to alter the structure of local hydration water. Our findings suggest that quick structure predictions can hint at IBS disparities that are borne out in more detail by simulations, leading us to posit that tools such as AlphaFold may be useful for preliminary IBS analysis in the context of AFP design campaigns that may begin with a large number of sequence candidates that must be narrowed down prior to in-depth characterization with simulations and experimental activity measurements. We hope these findings, combined with continuing advances in structure prediction tools, protein design methods, and simulation potentials, will support the development of a new generation of AFPs suitable for various practical applications requiring the modulation of ice growth.

Supporting Information Available

Additional figures showing structure prediction and simulation results and observations from the beta-solenoid design demonstration, as well as tables containing all model solenoid loop sequences and the top ProteinMPNN sequences, and representative inputs for our Amber simulations.

Acknowledgement

We thank Konrad Meister, Ilja Voets, and Renko de Vries for insightful discussions of ice-binding proteins and beta-solenoids, as well as all members of the Paesani Lab for continuous support and feedback. This research was supported by the Air Force Office of Scientific Research under award no. FA9550-20-1-0351. C.N.C. was supported by the San Diego Fellowship.

References

(1) Duman, J. G.; Olsen, T. M. Thermal hysteresis protein activity in bacteria, fungi, and phylogenetically diverse plants. *Cryobiology* **1993**, *30*, 322–328.

(2) DeVries, A. L.; Wohlschlag, D. E. Freezing resistance in some Antarctic fishes. *Science* **1969**, *163*, 1073–1075.

(3) Duman, J. G. The role of macromolecular antifreeze in the darkling beetle, Meracantha contracta. *J. Comp. Physiol.* **1977**, *115*, 279–286.

(4) Griffith, M.; Ala, P.; Yang, D. S.; Hon, W.-C.; Moffatt, B. A. Antifreeze protein produced endogenously in winter rye leaves. *Plant Physiol.* **1992**, *100*, 593–596.

(5) Devries, A. L. Glycoproteins as biological antifreeze agents in Antarctic fishes. *Science* **1971**, *172*, 1152–1155.

(6) Raymond, J. A.; DeVries, A. L. Adsorption inhibition as a mechanism of freezing resistance in polar fishes. *Proc. Natl. Acad. Sci. U.S.A.* **1977**, *74*, 2589–2593.

(7) Kristiansen, E.; Zachariassen, K. E. The mechanism by which fish antifreeze proteins cause thermal hysteresis. *Cryobiology* **2005**, *51*, 262–280.

(8) Knight, C. A.; De Vries, A. L.; Oolman, L. D. Fish antifreeze protein and the freezing and recrystallization of ice. *Nature* **1984**, *308*, 295–296.

(9) Knight, C. A.; Wen, D.; Laursen, R. A. Nonequilibrium antifreeze peptides and the recrystallization of ice. *Cryobiology* **1995**, *32*, 23–34.

(10) Rubinsky, B.; Arav, A.; Devries, A. The cryoprotective effect of antifreeze glycopeptides from antarctic fishes. *Cryobiology* **1992**, *29*, 69–79.

(11) Arav, A.; Rubinsky, B.; Fletcher, G.; Seren, E. Cryogenic protection of oocytes with antifreeze proteins. *Mol. Reprod. Dev.* **1993**, *36*, 488–493.

(12) Hirano, Y.; Nishimiya, Y.; Matsumoto, S.; Matsushita, M.; Todo, S.; Miura, A.; Komatsu, Y.; Tsuda, S. Hypothermic preservation effect on mammalian cells of type III antifreeze proteins from notched-fin eelpout. *Cryobiology* **2008**, *57*, 46–51.

(13) Halwani, D. O.; Brockbank, K. G.; Duman, J. G.; Campbell, L. H. Recombinant Dendroides canadensis antifreeze proteins as potential ingredients in cryopreservation solutions. *Cryobiology* **2014**, *68*, 411–418.

(14) Ekpo, M. D.; Xie, J.; Hu, Y.; Liu, X.; Liu, F.; Xiang, J.; Zhao, R.; Wang, B.; Tan, S. Antifreeze proteins: Novel applications and navigation towards their clinical application in cryobanking. *Int. J. Mol. Sci.* **2022**, *23*, 2639.

(15) Sirotinskaya, V.; Bar Dolev, M.; Yashunsky, V.; Bahari, L.; Braslavsky, I. Extended temperature range of the ice-binding protein activity. *Langmuir* **2024**, *40*, 7395–7404.

(16) Cutler, A. J.; Saleem, M.; Kendall, E.; Gusta, L. V.; Georges, F.; Fletcher, G. L. Winter flounder antifreeze protein improves the cold hardiness of plant tissues. *J. Plant Physiol.* **1989**, *135*, 351–354.

(17) Georges, F.; Saleem, M.; Cutler, A. J. Design and cloning of a synthetic gene for the flounder antifreeze protein and its expression in plant cells. *Gene* **1990**, *91*, 159–165.

(18) Holmberg, N.; Farrés, J.; Bailey, J. E.; Kallio, P. T. Targeted expression of a synthetic codon optimized gene, encoding the spruce budworm antifreeze protein, leads to accumulation of antifreeze activity in the apoplasts of transgenic tobacco. *Gene* **2001**, *275*, 115–124.

(19) Duman, J. G.; Wisniewski, M. J. The use of antifreeze proteins for frost protection in sensitive crop plants. *Environ. Exp. Bot.* **2014**, *106*, 60–69.

(20) Byass, L. Frozen confectionery product containing plant antifreeze protein. Unilever, assignee. Eur. *Pat. No. WO* **1998**, *98*, 04148.

(21) Clemmings, J. F.; Zoerb, H. F.; Rosenwald, D. R.; Huang, V. T. Method of making ice cream. 1997; US Patent 5,620,732.

(22) Regand, A.; Goff, H. D. Freezing and ice recrystallization properties of sucrose solutions containing ice structuring proteins from cold-acclimated winter wheat grass extract. *J. Food Sci.* **2005**, *70*, E552–E556.

(23) Kaleda, A.; Tsanev, R.; Klesment, T.; Vilu, R.; Laos, K. Ice cream structure modification by ice-binding proteins. *Food Chem.* **2018**, *246*, 164–171.

(24) Sicheri, F.; Yang, D. Ice-binding structure and mechanism of an antifreeze protein from winter flounder. *Nature* **1995**, *375*, 427–431.

(25) Sönnichsen, F. D.; DeLuca, C. I.; Davies, P. L.; Sykes, B. D. Refined solution structure

of type III antifreeze protein: hydrophobic groups may be involved in the energetics of the protein–ice interaction. *Structure* **1996**, *4*, 1325–1337.

(26) Liou, Y.-C.; Tocilj, A.; Davies, P. L.; Jia, Z. Mimicry of ice structure by surface hydroxyls and water of a β-helix antifreeze protein. *Nature* **2000**, *406*, 322–324.

(27) Graether, S. P.; Kuiper, M. J.; Gagné, S. M.; Walker, V. K.; Jia, Z.; Sykes, B. D.; Davies, P. L. β-Helix structure and ice-binding properties of a hyperactive antifreeze protein from an insect. *Nature* **2000**, *406*, 325–328.

(28) Graham, L. A.; Liou, Y.-C.; Walker, V. K.; Davies, P. L. Hyperactive antifreeze protein from beetles. *Nature* **1997**, *388*, 727–728.

(29) Tyshenko, M. G.; Doucet, D.; Davies, P. L.; Walker, V. K. The antifreeze potential of the spruce budworm thermal hysteresis protein. *Nat. Biotechnol.* **1997**, *15*, 887–890.

(30) Marshall, C. B.; Daley, M. E.; Graham, L. A.; Sykes, B. D.; Davies, P. L. Identification of the ice-binding face of antifreeze protein from Tenebrio molitor. *FEBS Lett.* **2002**, *529*, 261–267.

(31) Leinala, E. K.; Davies, P. L.; Doucet, D.; Tyshenko, M. G.; Walker, V. K.; Jia, Z. A β-helical antifreeze protein isoform with increased activity: Structural and functional insights. *J. Biol. Chem.* **2002**, *277*, 33349–33352.

(32) Garnham, C. P.; Campbell, R. L.; Davies, P. L. Anchored clathrate waters bind antifreeze proteins to ice. *Proc. Natl. Acad. Sci. U.S.A.* **2011**, *108*, 7363–7367.

(33) Hakim, A.; Nguyen, J. B.; Basu, K.; Zhu, D. F.; Thakral, D.; Davies, P. L.; Isaacs, F. J.; Modis, Y.; Meng, W. Crystal structure of an insect antifreeze protein and its implications for ice binding. *J. Biol. Chem.* **2013**, *288*, 12295–12304.

(34) Duboué-Dijon, E.; Laage, D. Comparative study of hydration shell dynamics around a hyperactive antifreeze protein and around ubiquitin. *J. Chem. Phys.* **2014**, *141*.

(35) Midya, U. S.; Bandyopadhyay, S. Hydration behavior at the ice-binding surface of the Tenebrio Molitor antifreeze protein. *J. Phys. Chem. B* **2014**, *118*, 4743–4752.

(36) Hudait, A.; Odendahl, N.; Qiu, Y.; Paesani, F.; Molinero, V. Ice-nucleating and antifreeze proteins recognize ice through a diversity of anchored clathrate and ice-like motifs. *J. Am. Chem. Soc.* **2018**, *140*, 4905–4912.

(37) Midya, U. S.; Bandyopadhyay, S. Role of polar and nonpolar groups in the activity of antifreeze proteins: A molecular dynamics simulation study. *J. Phys. Chem. B* **2018**, *122*, 9389–9398.

(38) Hudait, A.; Qiu, Y.; Odendahl, N.; Molinero, V. Hydrogen-bonding and hydrophobic groups contribute equally to the binding of hyperactive antifreeze and ice-nucleating proteins to ice. *J. Am. Chem. Soc.* **2019**, *141*, 7887–7898.

(39) Pal, P.; Chakraborty, S.; Jana, B. Deciphering the role of the non-ice-binding surface in the antifreeze activity of hyperactive antifreeze proteins. *J. Phys. Chem. B* **2020**, *124*, 4686–4696.

(40) Aich, R.; Pal, P.; Chakraborty, S.; Jana, B. Preferential ordering and organization of hydration water favor nucleation of ice by ice-nucleating proteins over antifreeze proteins. *J. Phys. Chem. B* **2023**, *127*, 6038–6048.

(41) Zhang, Y.; Wei, N.; Li, L.; Liu, Y.; Huang, C.; Li, Z.; Huang, Y.; Zhang, D.; Francisco, J. S.; Zhao, J.; Wang, C.; Zeng, X. C. Fully atomistic molecular dynamics simulation of ice nucleation near an antifreeze protein. *J. Am. Chem. Soc.* **2025**,

(42) Tyshenko, M. G.; d'Anjou, M.; Davies, P. L.; Daugulis, A. J.; Walker, V. K. Challenges in the expression of disulfide bonded, threonine-rich antifreeze proteins in bacteria and yeast. *Protein Expr. Purif.* **2006**, *47*, 152–161.

(43) Jumper, J.; Evans, R.; Pritzel, A.; Green, T.; Figurnov, M.; Ronneberger, O.; Tunyasuvunakool, K.; Bates, R.; Žídek, A.; Potapenko, A.; Bridgland, A.; Meyer, C.; Kohl, S. A. A.; Ballard, A. J.; Cowie, A.; Romera-Paredes, B.; Nikolov, S.; Jain, R.; Adler, J.; Back, T.; Petersen, S.; Reiman, D.; Clancy, E.; Zielinski, M.; Steinegger, M.; Pacholska, M.; Berghammer, T.; Bodenstein, S.; Silver, D.; Vinyals, O.; Senior, A. W.; Kavukcuoglu, K.; Kohli, P.; Hassabis, D. Highly accurate protein structure prediction with AlphaFold. *Nature* **2021**, *596*, 583–589.

(44) Baek, M.; DiMaio, F.; Anishchenko, I.; Dauparas, J.; Ovchinnikov, S.; Lee, G. R.; Wang, J.; Cong, Q.; Kinch, L. N.; Schaeffer, R. D.; Millán, C.; Park, H.; Adams, C.; Glassman, C. R.; DeGiovanni, A.; Pereira, J. H.; Rodrigues, A. V.; van Dijk, A. A.; Ebrecht, A. C.; Opperman, D. J.; Sagmeister, T.; Buhlheller, C.; Pavkov-Keller, T.; Rathinaswamy, M. K.; Dalwadi, U.; Yip, C. K.; Burke, J. E.; Garcia, K. C.; Grishin, N. V.; Adams, P. D.; Read, R. J.; Baker, D. Accurate prediction of protein structures and interactions using a three-track neural network. *Science* **2021**, *373*, 871–876.

(45) Lin, Z.; Akin, H.; Rao, R.; Hie, B.; Zhu, Z.; Lu, W.; dos Santos Costa, A.; Fazel-Zarandi, M.; Sercu, T.; Candido, S.; Rives, A. Language models of protein sequences at the scale of evolution enable accurate structure prediction. *bioRxiv* **2022**, doi: 10.1101/2022.07.20.500902.

(46) Dauparas, J.; Anishchenko, I.; Bennett, N.; Bai, H.; Ragotte, R. J.; Milles, L. F.; Wicky, B. I. M.; Courbet, A.; de Haas, R. J.; Bethel, N.; Leung, P. J. Y.; Huddy, T. F.; Pellock, S.; Tischer, D.; Chan, F.; Koepnick, B.; Nguyen, H.; Kang, A.; Sankaran, B.; Bera, A. K.; King, N. P.; Baker, D. Robust deep learning–based protein sequence design using ProteinMPNN. *Science* **2022**, *378*, 49–56.

(47) Alamdari, S.; Thakkar, N.; van den Berg, R.; Tenenholtz, N.; Strome, B.; Moses, A.;

Lu, A. X.; Fusi, N.; Amini, A. P.; Yang, K. K. Protein generation with evolutionary diffusion: Sequence is all you need. *bioRxiv* **2023**, doi: 10.1101/2023.09.11.556673.

(48) Watson, J. L.; Juergens, D.; Bennett, N. R.; Trippe, B. L.; Yim, J.; Eisenach, H. E.; Ahern, W.; Borst, A. J.; Ragotte, R. J.; Milles, L. F.; Wicky, B. I. M.; Hanikel, N.; Pellock, S. J.; Courbet, A.; Sheffler, W.; Wang, J.; Venkatesh, P.; Sappington, I.; Torres, S. V.; Lauko, A.; Bortoli, V. D.; Mathieu, E.; Ovchinnikov, S.; Barzilay, R.; Jaakkola, T. S.; DiMaio, F.; Baek, M.; Baker, D. De novo design of protein structure and function with RFdiffusion. *Nature* **2023**, *620*, 1089–1100.

(49) Abramson, J.; Adler, J.; Dunger, J.; Evans, R.; Green, T.; Pritzel, A.; Ronneberger, O.; Willmore, L.; Ballard, A. J.; Bambrick, J.; Bodenstein, S. W.; Evans, D. A.; Hung, C.-C.; O'Neill, M.; Reiman, D.; Tunyasuvunakool, K.; Wu, Z.; Žemgulytė, A.; Arvaniti, E.; Beattie, C.; Bertolli, O.; Bridgland, A.; Cherepanov, A.; Congreve, M.; Cowen-Rivers, A. I.; Cowie, A.; Figurnov, M.; Fuchs, F. B.; Gladman, H.; Jain, R.; Khan, Y. A.; Low, C. M. R.; Perlin, K.; Potapenko, A.; Savy, P.; Singh, S.; Stecula, A.; Thillaisundaram, A.; Tong, C.; Yakneen, S.; Zhong, E. D.; Zielinski, M.; Žídek, A.; Bapst, V.; Kohli, P.; Jaderberg, M.; Hassabis, D.; Jumper, J. M. Accurate structure prediction of biomolecular interactions with AlphaFold 3. *Nature* **2024**, *630*, 493–500.

(50) Chai Discovery team; Boitreaud, J.; Dent, J.; McPartlon, M.; Meier, J.; Reis, V.; Rogozhonikov, A.; Wu, K. Chai-I: Decoding the molecular interactions of life. *bioRxiv* **2024**, doi: 10.1101/2024.10.10.615955.

(51) Krishna, R.; Wang, J.; Ahern, W.; Sturmfels, P.; Venkatesh, P.; Kalvet, I.; Lee, G. R.; Morey-Burrows, F. S.; Anishchenko, I.; Humphreys, I. R.; McHugh, R.; Vafeados, D.; Li, X.; Sutherland, G. A.; Hitchcock, A.; Hunter, C. N.; Kang, A.; Brackenbrough, E.; Bera, A. K.; Baek, M.; DiMaio, F.; Baker, D. Generalized biomolecular modeling and design with RoseTTAFold All-Atom. *Science* **2024**, *384*, eadl2528.

(52) Wohlwend, J.; Corso, G.; Passaro, S.; Reveiz, M.; Leidal, K.; Swiderski, W.; Portnoi, T.; Chinn, I.; Silterra, J.; Jaakkola, T.; Barzilay, R. Boltz-I: Democratizing biomolecular interaction modeling. *bioRxiv* **2024**, doi: 10.1101/2024.11.19.624167.

(53) Hayes, T.; Rao, R.; Akin, H.; Sofroniew, N. J.; Oktay, D.; Lin, Z.; Verkuil, R.; Tran, V. Q.; Deaton, J.; Wiggert, M.; Badkundri, R.; Shafkat, I.; Gong, J.; Derry, A.; Molina, R. S.; Thomas, N.; Khan, Y. A.; Mishra, C.; Kim, C.; Bartie, L. J.; Nemeth, M.; Hsu, P. D.; Sercu, T.; Candido, S.; Rives, A. Simulating 500 million years of evolution with a language model. *Science* **2025**, *387*, 850–858.

(54) Bateman, A.; Murzin, A. G.; Teichmann, S. A. Structure and distribution of pentapeptide repeats in bacteria. *Protein Sci.* **1998**, *7*, 1477–1480.

(55) Hegde, S. S.; Vetting, M. W.; Roderick, S. L.; Mitchenall, L. A.; Maxwell, A.; Takiff, H. E.; Blanchard, J. S. A fluoroquinolone resistance protein from Mycobacterium tuberculosis that mimics DNA. *Science* **2005**, *308*, 1480–1483.

(56) MacDonald, J. T.; Kabasakal, B. V.; Godding, D.; Kraatz, S.; Henderson, L.; Barber, J.; Freemont, P. S.; Murray, J. W. Synthetic beta-solenoid proteins with the fragment-free computational design of a beta-hairpin extension. *Proc. Natl. Acad. Sci. U.S.A.* **2016**, *113*, 10346–10351.

(57) Yu, S. O. W. Antifreeze proteins: Activity comparisons and de novo design of an ice-binding protein. M.S. Thesis, Queen's University, 2010.

(58) Graether, S. P.; Jia, Z. Modeling pseudomonas syringae ice-nucleation protein as aβ-helical protein. *Biophys. J.* **2001**, *80*, 1169–1173.

(59) Garnham, C. P.; Campbell, R. L.; Walker, V. K.; Davies, P. L. Novel dimeric β-helical model of an ice nucleation protein with bridged active sites. *BMC Struct. Biol.* **2011**, *11*, 1–12.

(60) Forbes, J.; Bissoyi, A.; Eickhoff, L.; Reicher, N.; Hansen, T.; Bon, C. G.; Walker, V. K.; Koop, T.; Rudich, Y.; Braslavsky, I.; Davies, P. L. Water-organizing motif continuity is critical for potent ice nucleation protein activity. *Nat. Commun.* **2022**, *13*, 5019.

(61) Pal, P.; Pal, S.; Jana, B. Molecular insight of the ice nucleation by ice binding protein: A comparative study with ice nucleating protein, antifreeze protein, and non-ice-binding protein. *J. Phys. Chem. C* **2024**, *129*, 600–610.

(62) Kobashigawa, Y.; Nishimiya, Y.; Miura, K.; Ohgiya, S.; Miura, A.; Tsuda, S. A part of ice nucleation protein exhibits the ice-binding ability. *FEBS Lett.* **2005**, *579*, 1493–1497.

(63) Perkins, S. J. Protein volumes and hydration effects: the calculations of partial specific volumes, neutron scattering matchpoints and 280-nm absorption coefficients for proteins and glycoproteins from amino acid sequences. *Eur. J. Biochem.* **1986**, *157*, 169–180.

(64) Mirdita, M.; Schütze, K.; Moriwaki, Y.; Heo, L.; Ovchinnikov, S.; Steinegger, M. ColabFold: making protein folding accessible to all. *Nat. Methods* **2022**, *19*, 679–682.

(65) GEMMI. `https://project-gemmi.github.io/wasm/convert/cif2pdb.html`.

(66) Cock, P. J. A.; Antao, T.; Chang, J. T.; Chapman, B. A.; Cox, C. J.; Dalke, A.; Friedberg, I.; Hamelryck, T.; Kauff, F.; Wilczynski, B.; de Hoon, M. J. L. Biopython: Freely available Python tools for computational molecular biology and bioinformatics. *Bioinformatics* **2009**, *25*, 1422.

(67) Nguyen, H.; Roe, D. R.; Swails, J.; Case, D. A. PYTRAJ: Interactive data analysis for molecular dynamics simulations. *New Brunswick, NJ: Rutgers University* **2016**, 31.

(68) Roe, D. R.; Cheatham III, T. E. PTRAJ and CPPTRAJ: Software for processing and analysis of molecular dynamics trajectory data. *J. Chem. Theory Comput.* **2013**, *9*, 3084–3095.

(69) Case, D.; Aktulga, H.; Belfon, K.; Ben-Shalom, I.; Berryman, J.; Brozell, S.; Cerutti, D.; Cheatham, III, T.; Cisneros, G.; Cruzeiro, V.; Darden, T.; Duke, R.; Giambasu, G.; Gilson, M.; Gohlke, H.; Götz, A.; Harris, R.; Izadi, S.; Izmailov, S.; Kasavajhala, K.; Kaymak, M.; King, E.; Kovalenko, A.; Kurtzman, T.; Lee, T.; LeGrand, S.; Li, P.; Lin, C.; Liu, J.; Luchko, T.; Luo, R.; Machado, M.; Man, V.; Manathunga, M.; Merz, K.; Miao, Y.; Mikhailovskii, O.; Monard, G.; Nguyen, H.; O'Hearn, K.; Onufriev, A.; Pan, F.; Pantano, S.; Qi, R.; Rahnamoun, A.; Roe, D.; Roitberg, A.; Sagui, C.; Schott-Verdugo, S.; Shajan, A.; Shen, J.; Simmerling, C.; Skrynnikov, N.; Smith, J.; Swails, J.; Walker, R.; Wang, J.; Wang, J.; Wei, H.; Wolf, R.; Wu, X.; Xiong, Y.; Xue, Y.; York, D.; Zhao, S.; ; Kollman, P. *Amber 22*; University of California, San Francisco, United States-California, 2022.

(70) Case, D. A.; Cheatham III, T. E.; Darden, T.; Gohlke, H.; Luo, R.; Merz Jr, K. M.; Onufriev, A.; Simmerling, C.; Wang, B.; Woods, R. J. The Amber biomolecular simulation programs. *J. Comput. Chem.* **2005**, *26*, 1668–1688.

(71) Salomon-Ferrer, R.; Case, D. A.; Walker, R. C. An overview of the Amber biomolecular simulation package. *Wiley Interdiscip. Rev. Comput. Mol. Sci.* **2013**, *3*, 198–210.

(72) Le Grand, S.; Götz, A. W.; Walker, R. C. SPFP: Speed without compromise – A mixed precision model for GPU accelerated molecular dynamics simulations. *Comput. Phys. Commun.* **2013**, *184*, 374–380.

(73) Salomon-Ferrer, R.; Götz, A. W.; Poole, D.; Le Grand, S.; Walker, R. C. Routine microsecond molecular dynamics simulations with AMBER on GPUs. 2. Explicit solvent particle mesh Ewald. *J. Chem. Theory Comput.* **2013**, *9*, 3878–3888.

(74) Maier, J. A.; Martinez, C.; Kasavajhala, K.; Wickstrom, L.; Hauser, K. E.; Simmerling, C. ff14SB: Improving the accuracy of protein side chain and backbone parameters from ff99SB. *J. Chem. Theory Comput.* **2015**, *11*, 3696–3713.

(75) Horn, H. W.; Swope, W. C.; Pitera, J. W.; Madura, J. D.; Dick, T. J.; Hura, G. L.; Head-Gordon, T. Development of an improved four-site water model for biomolecular simulations: TIP4P-Ew. *J. Chem. Phys.* **2004**, *120*, 9665–9678.

(76) Ryckaert, J.-P.; Ciccotti, G.; Berendsen, H. J. Numerical integration of the cartesian equations of motion of a system with constraints: molecular dynamics of n-alkanes. *J. Comput. Phys.* **1977**, *23*, 327–341.

(77) Pettersen, E. F.; Goddard, T. D.; Huang, C. C.; Couch, G. S.; Greenblatt, D. M.; Meng, E. C.; Ferrin, T. E. UCSF Chimera – A visualization system for exploratory research and analysis. *J. Comput. Chem.* **2004**, *25*, 1605–1612.

(78) Hunter, J. D. Matplotlib: A 2D graphics environment. *Comput. Sci. Eng.* **2007**, *9*, 90–95.

(79) Waskom, M. L. Seaborn: Statistical data visualization. *J. Open Source Softw.* **2021**, *6*, 3021.

(80) Crooks, G. E.; Hon, G.; Chandonia, J.-M.; Brenner, S. E. WebLogo: A sequence logo generator. *Genome Res.* **2004**, *14*, 1188–1190.

(81) Pak, M. A.; Markhieva, K. A.; Novikova, M. S.; Petrov, D. S.; Vorobyev, I. S.; Maksimova, E. S.; Kondrashov, F. A.; Ivankov, D. N. Using AlphaFold to predict the impact of single mutations on protein stability and function. *PLoS ONE* **2023**, *18*, e0282689.

(82) Vega, C.; Sanz, E.; Abascal, J. The melting temperature of the most common models of water. *J. Chem. Phys.* **2005**, *122*.

(83) García Fernández, R.; Abascal, J. L.; Vega, C. The melting point of ice I_h for common water models calculated from direct coexistence of the solid-liquid interface. *J. Chem. Phys.* **2006**, *124*.

(84) Daley, M. E.; Spyracopoulos, L.; Jia, Z.; Davies, P. L.; Sykes, B. D. Structure and dynamics of a β-helical antifreeze protein. *Biochem.* **2002**, *41*, 5515–5525.

(85) Daley, M. E.; Sykes, B. D. The role of side chain conformational flexibility in surface recognition by Tenebrio molitor antifreeze protein. *Protein Sci.* **2003**, *12*, 1323–1331.

(86) Daley, M. E.; Sykes, B. D. Characterization of threonine side chain dynamics in an antifreeze protein using natural abundance 13 C NMR spectroscopy. *J. Biomol. NMR* **2004**, *29*, 139–150.

(87) Odendahl, N. Comparison of popular force fields for molecular modeling of proteins applied to ice binding of the Tenebrio molitor antifreeze protein. B.S. in Chemistry Honors Thesis, The University of Utah, 2016.

(88) Bennett, N. R.; Coventry, B.; Goreshnik, I.; Huang, B.; Allen, A.; Vafeados, D.; Peng, Y. P.; Dauparas, J.; Baek, M.; Stewart, L.; others Improving de novo protein binder design with deep learning. *Nat. Commun.* **2023**, *14*, 2625.

(89) Kajava, A. V.; Steven, A. C. β-rolls, β-helices, and other β-solenoid proteins. *Adv. Protein Chem.* **2006**, *73*, 55–96.

(90) Berman, H. M.; Westbrook, J.; Feng, Z.; Gilliland, G.; Bhat, T. N.; Weissig, H.; Shindyalov, I. N.; Bourne, P. E. The protein data bank. *Nucleic Acids Res.* **2000**, *28*, 235–242.

(91) Chen, C.; Bales, P.; Greenfield, J.; Heselpoth, R. D.; Nelson, D. C.; Herzberg, O. Crystal structure of ORF210 from E. coli O157: H1 phage CBA120 (TSP1), a putative tailspike protein. *PLoS ONE* **2014**, *9*, e93156.

(92) Chantigian, D. P.; Thoden, J. B.; Holden, H. M. Structural and biochemical characterization of a bifunctional ketoisomerase/N-acetyltransferase from Shewanella denitrificans. *Biochem.* **2013**, *52*, 8374–8385.

(93) Deng, X.; Gonzalez Llamazares, A.; Wagstaff, J. M.; Hale, V. L.; Cannone, G.; McLaughlin, S. H.; Kureisaite-Ciziene, D.; Löwe, J. The structure of bactofilin filaments reveals their mode of membrane binding and lack of polarity. *Nat. Microbiol.* **2019**, *4*, 2357–2368.

(94) Sharp, K. A. A peek at ice binding by antifreeze proteins. *Proc. Natl. Acad. Sci. U.S.A.* **2011**, *108*, 7281–7282.

(95) Gruneberg, A. K.; Graham, L. A.; Eves, R.; Agrawal, P.; Oleschuk, R. D.; Davies, P. L. Ice recrystallization inhibition activity varies with ice-binding protein type and does not correlate with thermal hysteresis. *Cryobiology* **2021**, *99*, 28–39.

(96) Vetting, M. W.; Hegde, S. S.; Hazleton, K. Z.; Blanchard, J. S. Structural characterization of the fusion of two pentapeptide repeat proteins, Np275 and Np276, from Nostoc punctiforme: Resurrection of an ancestral protein. *Protein Sci.* **2007**, *16*, 755–760.

(97) de Haas, R. J.; Tas, R. P.; van den Broek, D.; Zheng, C.; Nguyen, H.; Kang, A.; Bera, A. K.; King, N. P.; Voets, I. K.; de Vries, R. De novo designed ice-binding proteins from twist-constrained helices. *Proc. Natl. Acad. Sci. U.S.A.* **2023**, *120*, e2220380120.

(98) Lisanza, S. L.; Gershon, J. M.; Tipps, S. W.; Sims, J. N.; Arnoldt, L.; Hendel, S. J.; Simma, M. K.; Liu, G.; Yase, M.; Wu, H.; Tharp, C. D.; Li, X.; Kang, A.; Brackenbrough, E.; Bera, A. K.; Gerben, S.; Wittmann, B. J.; McShan, A. C.; Baker, D. Multistate and functional protein design using RoseTTAFold sequence space diffusion. *Nat. Biotechnol.* **2024**, 1–11.

(99) Saragovi, A.; Pyles, H.; Kwon, P.; Hanikel, N.; Dávila-Hernández, F. A.; Bera, A. K.; Kang, A.; Brackenbrough, E.; Vafeados, D. K.; Allen, A.; Stewart, L.; Baker, D. Controlling semiconductor growth with structured de novo protein interfaces. *bioRxiv* **2024**, doi: 10.1101/2024.06.24.600095.

(100) Peralta, M. D.; Karsai, A.; Ngo, A.; Sierra, C.; Fong, K. T.; Hayre, N. R.; Mirzaee, N.; Ravikumar, K. M.; Kluber, A. J.; Chen, X.; Liu, G.-y.; Toney, M. D.; Singh, R. R.; Cox, D. L. Engineering amyloid fibrils from β-solenoid proteins for biomaterials applications. *ACS Nano* **2015**, *9*, 449–463.

(101) Peng, Z.; Peralta, M. D.; Cox, D. L.; Toney, M. D. Bottom-up synthesis of protein-based nanomaterials from engineered β-solenoid proteins. *PLoS ONE* **2020**, *15*, e0229319.

(102) King, N. P.; Bale, J. B.; Sheffler, W.; McNamara, D. E.; Gonen, S.; Gonen, T.; Yeates, T. O.; Baker, D. Accurate design of co-assembling multi-component protein nanomaterials. *Nature* **2014**, *510*, 103–108.

(103) de Haas, R. J.; van Ossenbruggen, J.; van der Hoeven, J.; Timmermans, R. J.; Tas, R. P.; Voets, I. K.; de Vries, R. Flat solenoidal ice-binding proteins as scaffolds for solid-binders. *Adv. Mater. Interfaces* **2023**, *10*, 2300001.

(104) Radford, R. J.; Lawrenz, M.; Nguyen, P. C.; McCammon, J. A.; Tezcan, F. A. Porous protein frameworks with unsaturated metal centers in sterically encumbered coordination sites. *Chem. Commun.* **2011**, *47*, 313–315.

(105) Gonen, S.; DiMaio, F.; Gonen, T.; Baker, D. Design of ordered two-dimensional arrays mediated by noncovalent protein-protein interfaces. *Science* **2015**, *348*, 1365–1368.

(106) Heinz-Kunert, S. L.; Pandya, A.; Dang, V. T.; Tran, P. N.; Ghosh, S.; McElheny, D.; Santarsiero, B. D.; Ren, Z.; Nguyen, A. I. Assembly of π-stacking helical peptides into

a porous and multivariable proteomimetic framework. *J. Am. Chem. Soc.* **2022**, *144*, 7001–7009.

(107) Hess, S. S.; Coppola, F.; Dang, V. T.; Tran, P. N.; Mickel, P. J.; Oktawiec, J.; Ren, Z.; Král, P.; Nguyen, A. I. Noncovalent peptide assembly enables crystalline, permutable, and reactive thiol frameworks. *J. Am. Chem. Soc.* **2023**, *145*, 19588–19600.

(108) Govindarajan, A. G.; Lindow, S. E. Size of bacterial ice-nucleation sites measured in situ by radiation inactivation analysis. *Proc. Natl. Acad. Sci. U.S.A.* **1988**, *85*, 1334–1338.

(109) Southworth, M. W.; Wolber, P. K.; Warren, G. J. Nonlinear relationship between concentration and activity of a bacterial ice nucleation protein. *J. Biol. Chem.* **1988**, *263*, 15211–15216.

(110) Qiu, Y.; Hudait, A.; Molinero, V. How size and aggregation of ice-binding proteins control their ice nucleation efficiency. *J. Am. Chem. Soc.* **2019**, *141*, 7439–7452.

(111) Renzer, G.; de Almeida Ribeiro, I.; Guo, H.-B.; Fröhlich-Nowoisky, J.; Berry, R. J.; Bonn, M.; Molinero, V.; Meister, K. Hierarchical assembly and environmental enhancement of bacterial ice nucleators. *Proc. Natl. Acad. Sci. U.S.A.* **2024**, *121*, e2409283121.

(112) Thosar, A. U.; Cai, Y.; Marks, S. M.; Vicars, Z.; Choi, J.; Pallath, A.; Patel, A. J. On the engulfment of antifreeze proteins by ice. *Proc. Natl. Acad. Sci. U.S.A.* **2024**, *121*, e2320205121.

(113) Leinala, E. K.; Davies, P. L.; Jia, Z. Crystal structure of β-helical antifreeze protein points to a general ice binding model. *Structure* **2002**, *10*, 619–627.

(114) Pratt, O. S.; Elliott, L. G.; Haon, M.; Mesdaghi, S.; Price, R. M.; Simpkin, A. J.; Rigden, D. J. AlphaFold 2, but not AlphaFold 3, predicts confident but unrealistic β-solenoid structures for repeat proteins. *Comput. Struct. Biotechnol. J.* **2025**,

(115) Best, R. B.; de Sancho, D.; Mittal, J. Residue-specific α-helix propensities from molecular simulation. *Biophys. J.* **2012**, *102*, 1462–1467.

(116) Robustelli, P.; Piana, S.; Shaw, D. E. Developing a molecular dynamics force field for both folded and disordered protein states. *Proc. Natl. Acad. Sci.* **2018**, *115*, E4758–E4766.

(117) Petrov, D.; Zagrovic, B. Are current atomistic force fields accurate enough to study proteins in crowded environments? *PLoS Comput. Biol.* **2014**, *10*, e1003638.

(118) Qiu, Y.; Shan, W.; Zhang, H. Force field benchmark of amino acids. 3. Hydration with scaled Lennard-Jones interactions. *J. Chem. Inf. Model.* **2021**, *61*, 3571–3582.

(119) Shabane, P. S.; Izadi, S.; Onufriev, A. V. General purpose water model can improve atomistic simulations of intrinsically disordered proteins. *J. Chem. Theory Comput.* **2019**, *15*, 2620–2634.

(120) Tian, C.; Kasavajhala, K.; Belfon, K. A. A.; Raguette, L.; Huang, H.; Migues, A. N.; Bickel, J.; Wang, Y.; Pincay, J.; Wu, Q.; Simmerling, C. ff19SB: Amino-acid-specific protein backbone parameters trained against quantum mechanics energy surfaces in solution. *J. Chem. Theory Comput.* **2019**, *16*, 528–552.
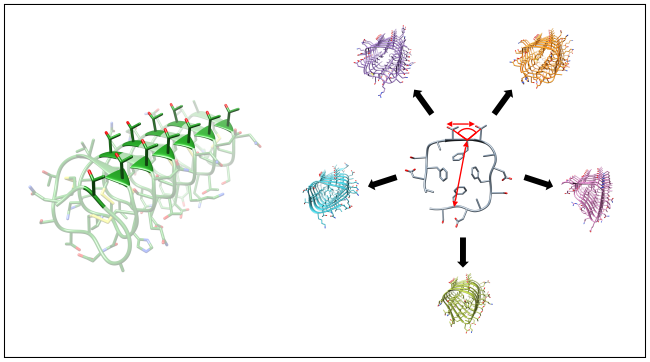
TOC Graphic